

# Ambipolar High Mobility Hexagonal Transistors on Hydrogen-Terminated Silicon (111) Surfaces

Binhui Hu,\* Mohamad M. Yazdanpanah, Joyce E. Coppock, and B. E. Kane  
*Laboratory for Physical Sciences, University of Maryland, College Park, Maryland 20740 and  
 Joint Quantum Institute, University of Maryland, College Park, Maryland 20742*  
 (Dated: September 15, 2015)

We have fabricated ambipolar transistors on chemically prepared hydrogen-terminated Si(111) surfaces, in which a two-dimensional electron system (2DES) or a two-dimensional hole system (2DHS) can be populated in the same conduction channel by changing the gate voltage of a global gate applied through a vacuum gap. Depending on the gate bias, ion implanted  $n^+$  and  $p^+$  regions function either as Ohmic contacts or as in-plane gates, which laterally confine the carriers induced by the global gate. On one device, electron and hole densities of up to  $7.8 \times 10^{11} \text{ cm}^{-2}$  and  $7.6 \times 10^{11} \text{ cm}^{-2}$  respectively are obtained. The peak electron mobility is  $1.76 \times 10^5 \text{ cm}^2/\text{Vs}$ , and the peak hole mobility is  $9.1 \times 10^3 \text{ cm}^2/\text{Vs}$  at 300 mK; the ratio of about 20 is mainly due to the very different valley degeneracies (6:1) of electrons and holes on the Si(111) surface. On another device, the peak electron mobility of  $2.2 \times 10^5 \text{ cm}^2/\text{Vs}$  is reached at 300 mK. These devices are hexagonal in order to investigate the underlying symmetry of the 2DESs, which have a sixfold valley degeneracy at zero magnetic field. Three magnetoresistance measurements with threefold rotational symmetry are used to determine the symmetry of the 2DESs at different magnetic field. At filling factor  $1 < \nu < 2$ , the observed anisotropy can be explained by a single valley pair occupancy of composite fermions (CFs). Qualitatively the CFs preserve the valley anisotropy, in addition to the twofold valley degeneracy. At magnetic field up to 35 T, the  $2/3$  fractional quantum Hall state is observed with a well developed hall plateau; at  $\nu < 2/3$ , the three magnetoresistances show a large anisotropy (50:1). We also show that device degradation is not a serious issue for our measurements, if the device is kept in vacuum or a nitrogen gas environment and its time in air is minimized.

## I. INTRODUCTION

Investigations of two-dimensional systems (2DSs) on Si surfaces began with metal-oxide-semiconductor field-effect transistors (MOSFETs) [1–5]. However, the amorphous  $\text{SiO}_2/\text{Si}$  interface severely limits the quality of the 2DSs. The development [6–10] of hydrogen-terminated silicon (111) [H-Si(111)] vacuum field effect transistors (FETs) is based on a simple but extraordinary fact: a wet chemical treatment of a Si(111) surface with an ammonium fluoride ( $\text{NH}_4\text{F}$ ) solution can produce an ideal H-passivated Si surface, which is both atomically flat and possesses a very low surface state density ( $\leq 10^{10} \text{ cm}^{-2}$ ) [11–14], leading to much higher carrier mobilities. In recent years, both a high quality two-dimensional electron system (2DES) with electron mobility of  $325,000 \text{ cm}^2/\text{Vs}$  [10] and a high quality two-dimensional hole system (2DHS) with hole mobility of  $10,000 \text{ cm}^2/\text{Vs}$  [9] have been realized in this system. They are comparable to the best Si/SiGe heterostructures [15–19], which are limited to the (100) oriented surfaces because of much higher threading dislocation densities on the other surface orientations [20, 21].

In this work we have fabricated ambipolar hexagonal devices, which can switch between a 2DES and a 2DHS in the same device by changing a gate voltage. Compared to other ambipolar devices [22–28], the 2DES on

the Si(111) surface has a sixfold valley degeneracy, while the valley degeneracy of holes is one. The ambipolar devices provide a direct comparison between electrons and holes with very different valley degeneracies in the same conduction channel, which allows a new perspective to the fundamental research, such as the properties of 2D metals [29]. In addition, the hexagonal devices enable the exploration of the sixfold valley-degenerate electron system.

In the H-Si(111) vacuum FET device, a global Si/SiO<sub>2</sub> gate piece is used to induce a 2DS, which is further confined into a well-defined 2D region by PN junction isolation and trench isolation. Similarly, future nanoelectronic devices, like quantum point contacts (QPCs) and quantum dots (QDs), may be realized on the Si(111) surfaces using the in-plane depleting gates based on PN junctions. Moreover, because of the sixfold valley degeneracy of the 2DES, the valley degree of freedom can provide extra resources for practical applications in the same way as spintronic devices utilize the spin degree of freedom. This will open up new opportunities for another class of devices — valleytronic devices [30–32].

The remainder of this paper is organized as follows. In Sec. II, we describe the device structure and operation principles, followed by detailed fabrication processes. In Sec. III, we characterize the devices to make sure that they work as intended, including surface topography measurement, a gate leakage check, PN junction isolation and leakage tests, and contact resistance measurements. In Sec. IV, we discuss the transport measurement results on these devices. We determined the 2D carrier mobilities in the experimentally accessible range of densities,

---

\* To whom correspondence should be addressed. Electronic mail: hubh@umd.edu

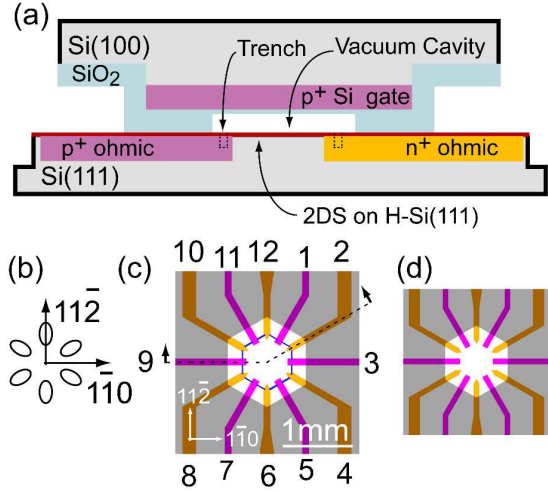


FIG. 1. (a) Schematic cross section of an ambipolar vacuum FET (not to scale), with a  $\text{SiO}_2/\text{Si}(100)$  remote gate piece and a  $\text{H-Si}(111)$  piece contact bonded in a vacuum. The remote gate piece is used to induce 2D carriers on the  $\text{H-Si}(111)$  surface by applying a gate voltage on a  $p^+$  gate layer through an encapsulated vacuum cavity. It also has a fully covered  $\text{SiO}_2$  layer with a thin layer of  $\text{SiO}_2$  ( $\sim 30$  nm) left in the cavity. (b) Six degenerated valleys of the 2DES with crystallographic orientations. (c) (d) In the  $\text{H-Si}(111)$  piece,  $n^+$  ( $p^+$ ) Ohmic contacts are used to access a 2DES (2DHS) at the center, with  $p^+$  ( $n^+$ ) regions acting as lateral confinement to restrict current flow between contacts to the hexagonal center 2DS. Two different configurations are investigated. (c) One has trench isolation, and (d) the other doesn't have trench isolation. The dash lines in (c) show the cross section depicted in (a).

which show that electron and hole mobilities are very different. Magnetotransport measurements show rich phenomena, including Shubnikov-de Haas (SdH) oscillations, integer quantum Hall effect (IQHE), fractional quantum Hall effects (FQHE) and large anisotropy in three magnetoresistance measurements at  $\nu < 2/3$ . In Sec. V, we discuss the device degradation with time and with exposure to ambient air, including the mobility deterioration and the increase of contact resistance. We conclude in Sec. VI with a discussion of further improvements and future directions.

## II. DEVICE STRUCTURE AND FABRICATION

The vacuum FET device is fabricated from two pieces. One is a  $\text{SiO}_2/\text{Si}(100)$  remote gate piece, and the other is a  $\text{H-terminated}$  high purity  $\text{Si}(111)$  piece, as shown in Fig. 1(a). Just like a MOSFET, when a positive (negative) gate voltage is applied between the remote gate and a  $n^+$  ( $p^+$ ) source Ohmic contact through an encapsulated vacuum cavity, a 2DES (2DHS) will be induced on the  $\text{H-Si}(111)$  surface. Since the 2DES has a sixfold valley degeneracy [Fig. 1(b)], the hexagonal device is designed to investigate its underlying symmetry, with six  $n^+$  Ohmic

contacts placed along the major axes of the constant energy ellipses on the  $\text{Si}(111)$  surface, labeled as 2,4,...,12. It also has six  $p^+$  Ohmic contacts placed between the  $n^+$  contacts, labeled as 1,3,...,11. The remote gate piece with a hexagonal cavity [Fig. 2 (b)] is contact bonded on the  $\text{H-Si}(111)$  piece in a vacuum chamber. When a positive (negative) gate voltage is applied, the  $n^+$  ( $p^+$ ) Ohmic contacts are used to access the 2DES (2DHS) at the center, and the  $p^+$  ( $n^+$ ) contacts act as lateral confinement. Figure 1 (b)-(d) show the arrangement of the  $n^+$  and  $p^+$  Ohmic contacts relative to crystallographic directions.

Two different types of devices are investigated. One has shallow trench isolation (STI) to confine the center 2DS [the center blue hexagon in Fig. 1(c)]; the other doesn't have the STI, and the center 2DS is defined by the hexagonal cavity [Fig. 1(d)]. There is typically a  $\sim 100$   $\mu\text{m}$  misalignment between the remote gate piece and the  $\text{H-Si}(111)$  piece when they are contact bonded. Because the distance between the trenches and the edges of the hexagonal cavity is more than  $200$   $\mu\text{m}$ , and the trenches are etched on the  $\text{Si}(111)$  piece, the misalignment doesn't change the center 2DS in the device with the STI; the misalignment can affect the center 2DS in the device without the STI when the  $n^+$  and  $p^+$  contacts are not concentric and aligned to the hexagonal cavity. However, the measurement results show that there is no significant difference between these two types of devices, because the relative placement of the contacts is fixed, and the bonding alignment is not critical in defining the device with the edges of the cavity far outside the contact perimeters. We have fabricated six devices (194-199) with peak electron mobilities of  $2.2 \times 10^5$   $\text{cm}^2/\text{Vs}$ ,  $5.6 \times 10^4$   $\text{cm}^2/\text{Vs}$ ,  $2.0 \times 10^5$   $\text{cm}^2/\text{Vs}$ ,  $5.2 \times 10^4$   $\text{cm}^2/\text{Vs}$ ,  $1.76 \times 10^5$   $\text{cm}^2/\text{Vs}$  and  $5.8 \times 10^4$   $\text{cm}^2/\text{Vs}$  at  $300$  mK respectively, in which four (194-197) of them have the STI, and the other two (198,199) do not have it. Most data presented here are from two devices, sample 194 (with the STI) and sample 198 (without the STI).

### A. Gate piece

The remote gate piece is fabricated from a  $\text{Si}(100)$  wafer (float zone,  $\text{Si:B}$ , resistivity  $> 10,000\Omega\cdot\text{cm}$ ). First, a  $p^+$  gate conducting layer is formed by ion implantation with  $2.4 \times 10^{15}$   $\text{cm}^{-2}$ ,  $15$  keV boron ions, as shown in Fig. 1(a). Then a  $2$   $\mu\text{m}$  deep Si mesa is dry etched around the edges of each die using reactive ion etching (RIE). Next, a  $\sim 350$  nm thick  $\text{SiO}_2$  layer is thermally grown on the top: dry oxidation at  $1050$   $^\circ\text{C}$  for  $15$  min, followed by wet oxidation at  $1050$   $^\circ\text{C}$  for  $27$  min and another dry oxidation at  $1050$   $^\circ\text{C}$  for  $10$  min. The dry-wet-dry cycle is used to improve the gate oxide quality, and also activates the implanted dopants. After that, a cavity with a  $\sim 30$  nm thick oxide layer left behind is formed by dry etching and wet etching. In order to make sure the oxide thickness is reduced to  $\sim 30$  nm in the cavity, a test wafer

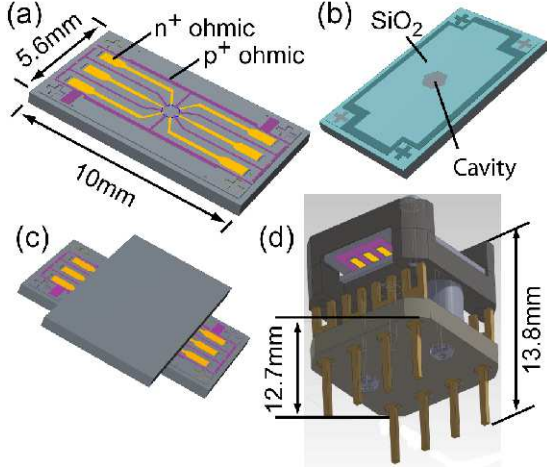


FIG. 2. (a) A H-Si(111) piece with six  $n^+$  contacts (yellow) and six  $p^+$  contacts (purple). (b) A Si/SiO<sub>2</sub> remote gate piece which is fully covered by SiO<sub>2</sub>, except the two grey crosses where the gate contacts are made. There is a  $\sim 30$  nm oxide at the bottom of the hexagonal cavity. (c) 3D view of a bonded device. (d) A bonded device placed in a customized holder and installed on an 8-pin dual in-line package (DIP) header without wiring.

and the device wafer are loaded into a RIE machine and dry etched at the same time. Both have the same  $\sim 350$  nm thick oxide layer, and the oxide layer is dry etched by  $\sim 270$  nm. Then the depth of the cavity in the test wafer is measured using a profilometer after removing photoresist. The time of the wet etching to leave the  $\sim 30$  nm thick oxide layer is calculated based on the oxide thickness, the depth of the cavity and the wet etching rate. The fully SiO<sub>2</sub> encapsulated gate piece with the oxide reduced cavity drastically reduces the likelihood of gate leakage, compared to the gate piece where the doped regions were exposed. We have tested remote gate pieces with either  $\sim 350$  nm or  $\sim 200$  nm thick thermal oxide, and both of them work well. Finally, the wafer is diced into  $5.6 \times 10$  mm<sup>2</sup> remote gate pieces, as shown in Fig. 2 (b).

### B. Si(111) piece

The H-Si(111) piece is also  $5.6 \times 10$  mm<sup>2</sup> made from a  $p^-$  high purity Si(111) wafer (float zone, resistivity  $> 10,000\Omega\cdot\text{cm}$ ). First, a 30 nm thick sacrificial SiO<sub>2</sub> layer is thermally grown on the top of the Si(111) substrate by dry oxidation at 950 °C for 30 min in a CMOS grade furnace to reduce the channeling effect during ion implantation and protect the clean Si(111) surface. Next, the six  $n^+$  contact regions are patterned by photolithography with the primary flat of the Si(111) wafer (oriented to [112] [33]) aligned ( $< 5^\circ$ ) along the long side of the dies. Then the wafer is ion implanted with  $4.5 \times 10^{14}$  cm<sup>-2</sup> phosphorus ions at 50 keV. Alignment marks are

formed at the same time. Similarly, the six  $p^+$  contact regions are defined by photolithography and ion implantation with  $9 \times 10^{14}$  cm<sup>-2</sup> boron ions at an energy of 15 keV. The ion implantation parameters are based on previous works [6, 9] and simulation results from SUPREM-IV process simulator [34]. The parameters are selected so that after thermal annealing, the peak doping concentration is located near the Si(111) surface, and about one order of magnitude higher than that of the three-dimensional (3D) metal-insulate transition (MIT), as shown in Fig. 9. (The 3D MIT occurs at doping concentration of  $3.74 \times 10^{18}$  cm<sup>-3</sup> for phosphorus [35] and  $3.95 \times 10^{18}$  cm<sup>-3</sup> for boron [36].) After each ion implantation, the photoresist is removed by acetone cleaning and piranha cleaning. First the wafer is immersed in boiling acetone for 30 min to remove most of the photoresist. Then the wafer is rinsed with isopropyl alcohol (IPA) and de-ionized (DI) water. Next, the wafer is immersed in a piranha solution (4 H<sub>2</sub>SO<sub>4</sub>(98%) : 1 H<sub>2</sub>O<sub>2</sub> (30%)) at 100 °C for 30 min to remove the residual photoresist. Right before rapid thermal annealing (RTA), the wafer is RCA-1 cleaned for 5 min with a H<sub>2</sub>O<sub>2</sub>/NH<sub>4</sub>OH/H<sub>2</sub>O solution, then thoroughly rinsed in DI water, and spin-dried. The wafer is annealed in a CMOS grade rapid thermal annealer at 950 °C for 60 sec. Alignment marks from ion implantations are visible before the RTA process, but invisible after it. RCA-1 clean etches the ion implanted SiO<sub>2</sub> regions before the RTA process. They serve as alignment marks to do mesa etching, but the contrast is very low. It is helpful to define global alignment marks before the RTA process using CMOS compatible processes. Next, if STI is desired, the 200 nm deep and 10  $\mu\text{m}$  wide shallow trenches are formed by dry etching. After that, a 2  $\mu\text{m}$  deep Si mesa is dry etched around the edges of each die. This mesa prevents particles from accumulating on the surface while handling the substrate and ensures a clean edge for bonding [6]. It also defines each die for dicing. Finally, the wafer is diced into individual Si(111) pieces, as shown in Fig. 2(a).

### C. Bonding and wiring

After standard cleaning (acetone cleaning, IPA rinse, DI water rinse, piranha cleaning, and DI water rinse) in clean room, one Si(111) piece and one Si/SiO<sub>2</sub> remote gate piece are transferred into an oxygen-free glove box with a typical O<sub>2</sub> concentration of 2 ppm. The Si(111) piece is put in a diluted solution of HF/H<sub>2</sub>O (1:20) for 2 min to remove the sacrificial SiO<sub>2</sub> layer, and then immersed in a 40% NH<sub>4</sub>F solution for 10 min to create an atomically flat H-passivated Si(111) surface, with DI water rinse after each step. It is crucial that each of these solutions is oxygen-free to ensure the high quality of the final device [37]. Usually they are deoxygenated with a constant agitation from a magnetic stir rod for 72 hours in the glove box. Finally, these two pieces are transferred into a vacuum chamber, and pushed against a sapphire

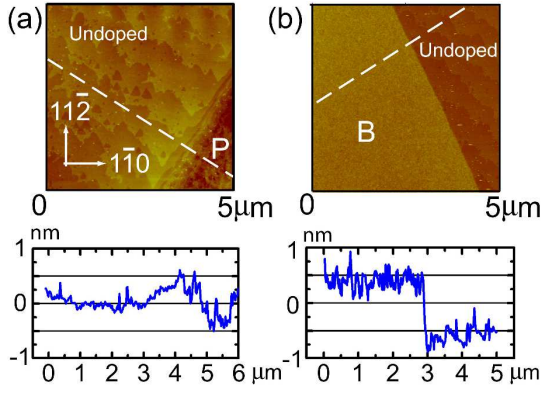


FIG. 3. AFM images of a H-Si(111) surface with (a) a phosphorus-doped contact edge and (b) a boron-doped contact edge. They also show atomic steps in undoped areas and the crystallographic directions. Bottom graphs show height profiles along white dash lines in the top graphs.

boss to apply a pressure between them, sufficient to initiate bonding through van der Waals forces.

The bonded device is loosely placed in a customized holder machined from polyimide material, which is designed to facilitate handling of the device without applying stress. It is wired in a nitrogen glove box by hand soldering using indium at 320 °C and installed on a standard 8-pin dual in-line package (DIP) header, which is compatible with sample holders at the National High Magnetic Field Laboratory (NHMFL). If only the 2DES is to be investigated, eight contacts are sufficient, including two gate contacts and six Ohmic contacts to the 2DES. There are 12 wires in our cryostat. In order to measure both the 2DES and the 2DHS, the 8 pin DIP header is inserted into another 20 pin DIP header, and four Ohmic contacts to the 2DHS are directly wired to the 20 pin DIP header. Two  $p^+$  Ohmic contacts 3, 9 are not wired. The wired sample is transferred from the nitrogen glove box to the cryostat, and the cryostat is pumped to vacuum ( $p < 10^{-3}$  mbar) in less than one hour. Figure 2(d) shows one of the final devices without wiring. Similar fabrication processes have been discussed elsewhere in detail [38, 39].

### III. DEVICE CHARACTERIZATION

#### A. Topography

Because the Si(111) piece and the Si/SiO<sub>2</sub> remote gate piece are contact bonded through van der Waals forces, successful bonding requires that the surfaces are clean, flat and smooth. Atomic force microscopy (AFM) is used to investigate the topography of the Si(111) surface, particularly the differences in height and flatness of doped and undoped areas. Figure 3 shows that the Si(111) surface is clean with atomic steps. Typically the doped contacts on the Si(111) surface are at different ele-

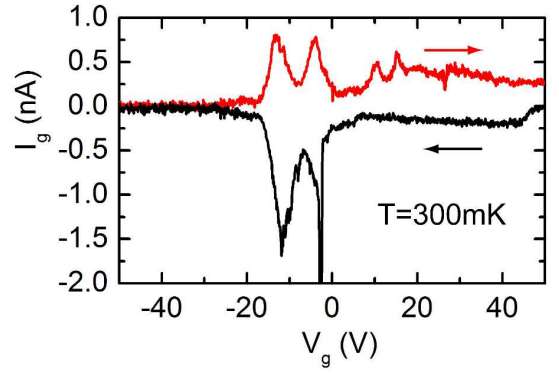


FIG. 4. Gate current  $I_g$  vs. gate voltage  $V_g$  on sample 198 when  $V_g$  is swept between -50 V ( $p_{2d} = 7.6 \times 10^{11} \text{ cm}^{-2}$ ) and 50 V ( $n_{2d} = 7.8 \times 10^{11} \text{ cm}^{-2}$ ) at a sweep rate of 0.2 V/s with all wired  $n^+$ ,  $p^+$  contacts grounded. Arrows indicate the voltage sweep direction. Current peaks at  $V_g \sim -12$  V and -3 V are due to the formation or depletion of 2DSs.  $I_g \sim 0.5$  nA is from the gate capacitance.

vations from the undoped Si(111) surface after wet chemical cleaning and passivation. Specifically,  $n^+$  Ohmic contacts (phosphorus doped) are  $\sim 1$  nm below the undoped region, as shown in Fig. 3(a);  $p^+$  Ohmic contacts (boron doped) are  $\sim 1.5$  nm above the undoped region, as shown in Fig. 3(b). We have found that the RCA-1 clean with a H<sub>2</sub>O<sub>2</sub>/NH<sub>4</sub>OH/H<sub>2</sub>O solution etches the SiO<sub>2</sub> region exposed to ion implantation much faster than the unimplanted oxide region. Once it etches through the sacrificial oxide layer completely, it etches the underlying doped silicon. This results in larger height difference, which may impair the Ohmic contact to the 2DS. Therefore, the time in the RCA-1 clean should be minimized, and under 20 minutes [39]. Piranha clean with a H<sub>2</sub>SO<sub>4</sub>/H<sub>2</sub>O<sub>2</sub> solution does not have this issue and thus is preferred when cleaning Si(111) pieces.

#### B. Gate leakage

Samples are intended for measurements at low temperature; consequently even sub-nanoampere gate leakage can potentially affect the data. All electrical measurements made in this section (Sec. III) were performed at  $T = 300$  mK in a helium 3 refrigerator (Oxford Instruments, HelioxVL). Gate leakage was checked when all Ohmic contacts were grounded and the gate voltage  $V_g$  was swept between -50 V ( $p_{2d} = 7.6 \times 10^{11} \text{ cm}^{-2}$ ) and 50V ( $n_{2d} = 7.8 \times 10^{11} \text{ cm}^{-2}$ ) at a sweep rate of 0.2 V/sec. The measured gate current was less than 0.5 nA at -50 V  $< V_g < -20$  V and 0 V  $< V_g < 50$  V, as shown in Fig. 4. (The capacitance between the gate and the ground was measured to be about 3 nF, so the gate current of 0.6 nA was expected.) The static leakage current was less than 50 pA at  $V_g = \pm 50$  V. There is no measurable leakage current for these devices. In Fig. 4, the peak current at  $V_g \sim -12$  V and -3 V is due to the formation or depletion



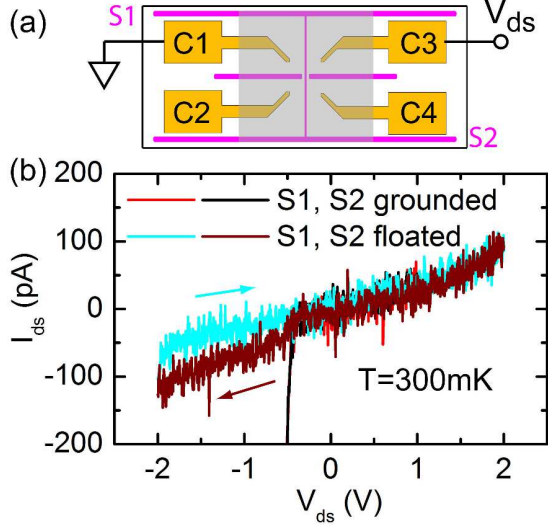


FIG. 5. (a) A test device with four  $n^+$  Ohmic contacts (yellow) and  $p^+$  isolation lines (purple). A center vertical  $p^+$  isolation line separates the 2DES (shaded area) into two halves. (b) Leakage current  $I_{ds}$  vs.  $V_{ds}$  at  $n_{2d} = 6 \times 10^{11} \text{ cm}^{-2}$  with either  $p^+$  isolation lines (S1, S2) grounded or floated. The leakage due to forward biasing happens at  $V_{ds} < -0.4 \text{ V}$  when S1, S2 are grounded. Arrows show the voltage sweep direction.

of the 2DES or 2DHS.

### C. PN junction isolation and leakage

In earlier generation devices, a silicon-on-insulator (SOI) remote gate piece was used to define the 2DS on the H-Si(111) surface with a shield layer to restrict the electric field of the gate [6]. With the introduction of the Si/SiO<sub>2</sub> global gate, the electric field is all over the H-Si(111) surface, as shown in Fig.1 (c) (d). PN junction isolation and trench isolation are used to confine the 2DS. Using the SUPREM-IV process simulator, the depth of the  $p^+$  and  $n^+$  Ohmic contacts, defined as the region where doping concentration is higher than that of the 3D MIT ( $\sim 4 \times 10^{18} \text{ cm}^{-3}$  [35, 36]), is determined to be about 100 nm, as shown in Fig. 9(a)(b). For the trench isolation, 200 nm deep and 10  $\mu\text{m}$  wide trenches are used. Since the depth of the 2DS is less than 10 nm for 2D carrier density higher than  $10^{11} \text{ cm}^{-2}$  in the H-Si(111) vacuum FET [40, 41], both PN junction isolation and trench isolation should work well.

A test device [Fig. 5(a)] was fabricated to verify the effectiveness of the PN junction isolation. A 2DES [shaded area in Fig. 5(a)] is separated by a 10  $\mu\text{m}$  wide boron ion-implanted line (the vertical line). At an electron density of  $6 \times 10^{11} \text{ cm}^{-2}$ , the resistance between  $n^+$  contacts C1 and C3 were measured, while  $p^+$  contacts S1 and S2 were either grounded or floated. In both cases, Fig. 5(b) shows that the resistance between C1 and C3 was larger than 25

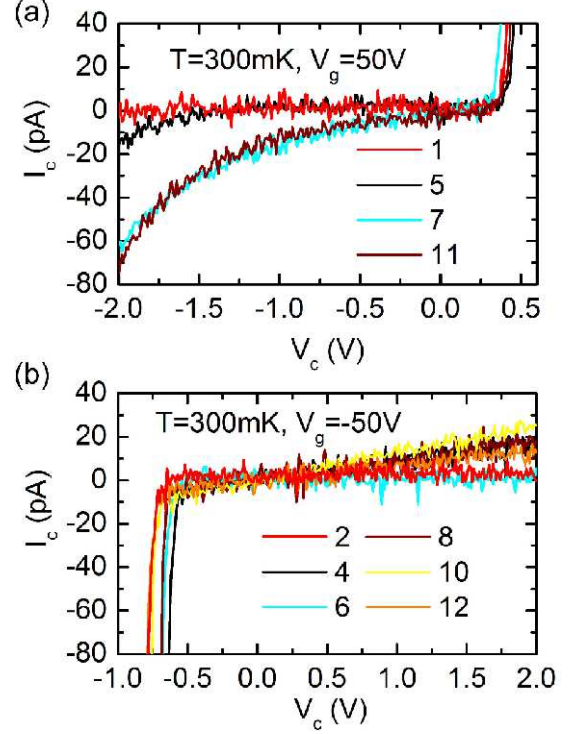


FIG. 6. PN junction leakage current on sample 198. (a)  $P^+$  contact leakage current  $I_c$  at  $V_g = 50 \text{ V}$  ( $n_{2d} = 7.8 \times 10^{11} \text{ cm}^{-2}$ ) when a voltage  $V_c$  is applied at each wired  $p^+$  contact, while all  $n^+$  contacts are grounded. (b)  $N^+$  contact leakage current  $I_c$  at  $V_g = -50 \text{ V}$  ( $p_{2d} = 7.6 \times 10^{11} \text{ cm}^{-2}$ ) when  $V_c$  is applied at each  $n^+$  contact, while all wired  $p^+$  contacts are grounded. In both cases, the resistance is larger than 100 G $\Omega$  at  $-0.5 < V_c < 0.4 \text{ V}$ .

G $\Omega$  at  $-0.2 < V_{ds} < 1 \text{ V}$ , likely dominated by inter-wire leakage, so the PN junction isolation is effective. When S1 and S2 were grounded, the PN junction began to leak at  $V_{ds} = -0.4 \text{ V}$  because of forward bias.

For the device under investigation (sample 198), we also measured the PN junction leakage current. At an electron density of  $7.8 \times 10^{11} \text{ cm}^{-2}$ , the leakage current from  $p^+$  contacts 1, 5, 7, 11 to the 2DES was measured by applying a voltage  $V_c$  at each contact, while all  $n^+$  contacts were grounded. (Here  $p^+$  contacts 3, 9 were not wired, and thus floated.) The resistance was larger than 100 G $\Omega$  at  $-0.5 < V_c < 0.4 \text{ V}$ , as shown in Fig. 6(a). Similarly, the leakage current from  $n^+$  contacts 2, 4, 6, 8, 10, 12 to the 2DHS was measured by applying a voltage  $V_c$  at each  $n^+$  contact, while all wired  $p^+$  contacts were grounded. Figure 6(b) shows that the resistance was also larger than 100 G $\Omega$  at  $-0.5 < V_c < 1 \text{ V}$ . In our transport measurements, lateral confining gates were floated with respect to the 2DS, and the source-drain voltage is less than  $\pm 0.1 \text{ V}$  with the source-drain current equal or larger than 10 nA, so the leakage current from the PN junction isolation has only a negligible effect on the measurements.

We also measured the conductance between  $n^+$  contacts C1 and C2 while negatively biasing  $p^+$  contacts S1

and S2. The results show that the conductance decreases with increasing negative bias voltage, which suggests that depletion is occurring and reverse biasing lateral gates to confine carriers should be possible.

#### D. Ohmic contacts

Contacts to the 2DSs on H-Si(111) surfaces have been problematic especially at low temperature ( $< 1$  K) and low carrier density, which limits the lowest accessible 2D carrier density in experiments. The main issues are large contact resistances (on the order of  $1$  M $\Omega$ ) and nonlinearity in current-voltage (IV) curves [38].

For the device without STI, the contact problem can be mitigated by the presence of  $\text{SiO}_2$  over the contact regions. At the center 2DS region, the dielectric is vacuum with a dielectric constant of 1; at the contact regions,  $\text{SiO}_2$  is the dielectric with a dielectric constant of 3.9. So at the same gate voltage, the contact regions have about four times higher carrier density than the center 2DS region when the threshold voltages are negligible, and the contact resistance is reduced.

The contact resistance was measured at  $T = 300$  mK, using a homemade voltage amplifier with input bias current  $\sim 1$  pA and input impedance  $> 200$  G $\Omega$ . Figure 7(a) shows the circuit diagram measuring contact 6, where current  $I_{ds}$  is injected from contact 12 to contact 6, and voltage  $V_d$  is measured between contacts 2 and 6. The IV curves were nonlinear at  $V_g = 5$  V ( $n_{2d} = 0.87 \times 10^{11} \text{ cm}^{-2}$ ) and became linear at  $V_g = 6$  V ( $n_{2d} = 1.02 \times 10^{11} \text{ cm}^{-2}$ ), as shown in Fig. 7(b). So the lowest accessible 2D electron density was about  $0.9 \times 10^{11} \text{ cm}^{-2}$  at 300 mK for this device. Figure 7(c) shows contact resistance  $R_c$  as a function of gate voltage  $V_g$ . The sheet resistance of the  $n^+$  regions was measured to be  $129 \text{ } \Omega/\square$  at 4.2 K, and this 3D metallic resistance should not change too much at 300 mK because of the lack of phonon scattering with the doping concentration well above the 3D MIT density. The  $n^+$  contact resistance is calculated to be about  $2.5 \text{ k}\Omega$  if only considering this sheet resistance, which is much smaller than the measured contact resistance at  $V_g < 10$  V. The commercial software package COMSOL Multiphysics [42] is used to calculate the contact resistance including both the  $n^+$  contact regions and the 2DES region. For example, at  $V_g = 10$  V, the sheet resistances of the  $n^+$  contact regions and the 2DES region are  $129 \text{ } \Omega/\square$  and  $807 \text{ } \Omega/\square$  respectively, and the calculated contact resistance is about  $2.9 \text{ k}\Omega$ , which is significantly less than measured contact resistance of  $4.9 \text{ k}\Omega$ . The difference is likely related to the highly resistive transition region between the metallic  $n^+$  contact and the 2DES, where the doping concentration is less than the 3D MIT density ( $\sim 3.74 \times 10^{18} \text{ cm}^{-3}$  [35]), as shown in Fig. 9(a). The 2DES in the transition region can undergo a 2D MIT and become an insulator at low carrier density and low temperature, resulting in high contact resistance [43].

The  $p^+$  contact resistance was also measured. Figure

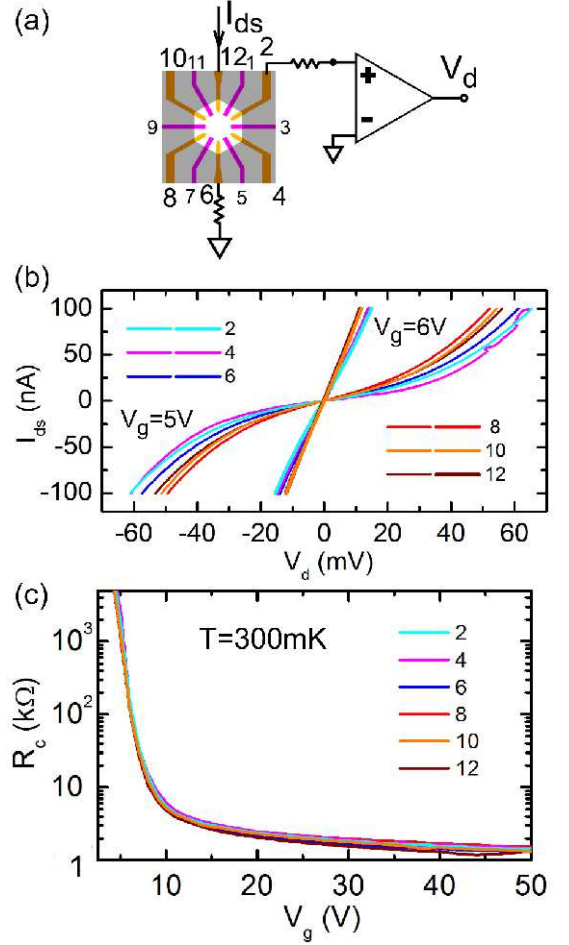


FIG. 7.  $n^+$  contacts on sample 198 measured at 300 mK. (a) Circuit diagram measuring contact 6, with current  $I_{ds}$  injected from contact 12 to contact 6 and voltage  $V_d$  measured between contacts 2 and 6. (b) Current-voltage curves of  $n^+$  contacts at  $V_g = 5$  V ( $n_{2d} = 0.87 \times 10^{11} \text{ cm}^{-2}$ ) and  $6$  V ( $n_{2d} = 1.02 \times 10^{11} \text{ cm}^{-2}$ ). (c) Contact resistance  $R_c$  as a function of gate voltage  $V_g$ . At  $V_g < 6$  V,  $R_c$  is calculated when  $|I_{ds}| \leq 4$  nA; otherwise,  $R_c$  is determined at  $|I_{ds}| \leq 100$  nA.

8(a) shows that the IV curves were nonlinear at  $V_g = -20$  V ( $p_{2d} = 2.94 \times 10^{11} \text{ cm}^{-2}$ ) and became linear at  $V_g = -25$  V ( $p_{2d} = 3.72 \times 10^{11} \text{ cm}^{-2}$ ), which is much higher than the corresponding gate voltage for the  $n^+$  contacts. The lowest accessible 2D hole density was about  $3 \times 10^{11} \text{ cm}^{-2}$  at 300 mK. Figure 8(b) shows contact resistance  $R_c$  as a function of gate voltage  $V_g$ . We measured the sheet resistance of the  $p^+$  regions to be  $103 \text{ } \Omega/\square$  at 4.2 K, which is comparable to the  $n^+$  regions. If we compare the doping profile of the phosphorus doped region and the boron doped region (Fig. 9), especially the top  $\sim 10$  nm area where 2DSs are populated, there is no significant difference. It is quite puzzling why the  $p^+$  contacts are much worse than the  $n^+$  contacts.

There are probably two reasons. One is that electrons have much stronger Coulomb disorder screening strength

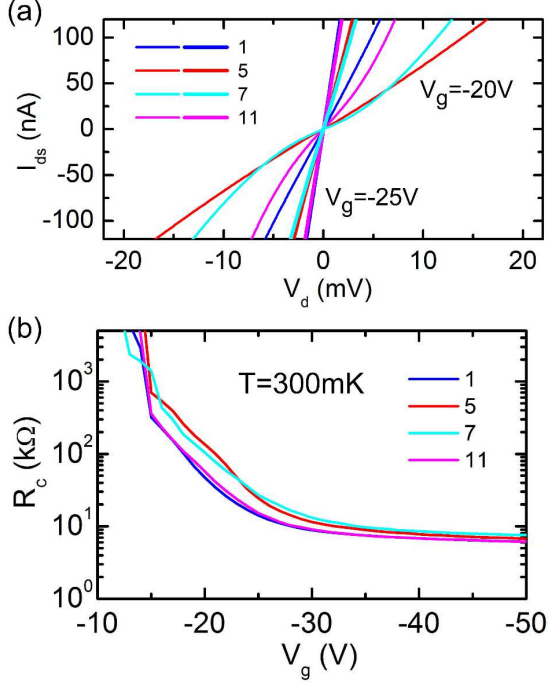


FIG. 8.  $P^+$  contacts on sample 198 measured at 300 mK. (a) Current-voltage curves of  $p^+$  contacts at  $V_g = -20$  V ( $p_{2d} = 2.94 \times 10^{11} \text{ cm}^{-2}$ ) and  $-25$  V ( $p_{2d} = 3.72 \times 10^{11} \text{ cm}^{-2}$ ). (b) Contact resistance  $R_c$  as a function of gate voltage  $V_g$ . At  $-V_g < 25$  V,  $R_c$  is calculated when  $|I_{ds}| \leq 4$  nA; otherwise,  $R_c$  is determined at  $|I_{ds}| \leq 100$  nA.

than holes due to the very different valley degeneracy (6:1) [29]; the other is that there could be very different lateral defect profiles, such as end-of-range (EOR) dislocation loops [44]. The very different defect profiles can be caused by two reasons: first, phosphorus and boron ions have very different critical doses for amorphization of silicon [45]. At room temperature, the critical dose of phosphorus ions is  $\sim 10^{15} \text{ cm}^{-2}$ , about twice as high as the dose used here; while it is  $\sim 10^{17} \text{ cm}^{-2}$  for boron ions, which is about 100 times higher than the current dose. It is often easier to regrow the crystal from an amorphous layer via solid state epitaxy (activation energy  $\sim 2.3$  eV in Silicon) than it is to anneal out defects (activation energy  $\sim 5$  eV). Thus, two schemes for ion implantation are usually used: either perform ion implantation above the critical dose and use low temperature annealing to regrow material or perform ion implantation below the critical dose and use high temperature annealing to get rid of defects [44]. Second, phosphorus and boron ions have different mask edge effects, such as lateral straggle and shadowing effect, resulting in different lateral doping profile [46, 47].

It is probably beneficial to do the ion implantation at higher dose and cryogenic temperature. We observed improvement of the  $p^+$  contacts when the dose of the boron ion implantation was increased from  $6 \times 10^{14} \text{ cm}^{-2}$  to  $2.4 \times 10^{15} \text{ cm}^{-2}$ , then the contacts were annealed at

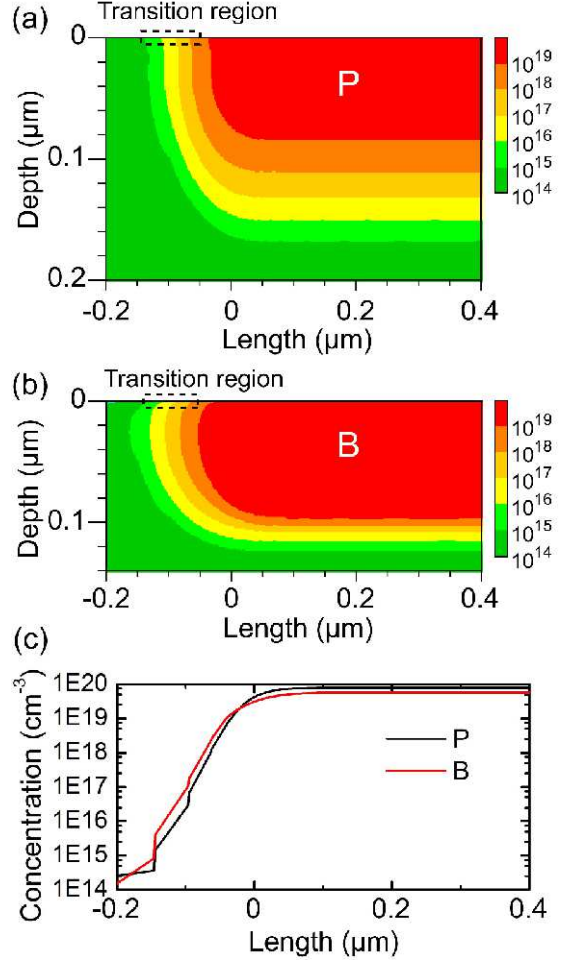


FIG. 9. 2D doping profile of (a) phosphorus-doped region and (b) boron-doped region in Si using SUPREM-IV simulator. In (a),  $4.5 \times 10^{14} \text{ cm}^{-2}$ , 50 keV phosphorus ions are implanted through a 30 nm oxide; in (b),  $9 \times 10^{14} \text{ cm}^{-2}$ , 15 keV boron ions are implanted through a 30 nm oxide. Both are annealed at  $950^\circ \text{C}$  for 1 min. Ions are implanted at  $0^\circ$  with vertical photoresist edge at Length=0. (c) Doping concentrations of phosphorus and boron along the Si surface at (a) and (b).

$1000^\circ \text{C}$  for 10 min [9]. But there is a possibility that the contact bonding could be difficult, because of the larger height difference between the  $p^+$  contact region and the undoped region after wet chemical etching than that shown in Fig. 3 (b). In order to access lower 2D carrier densities, a structure like a bi-layer gate structure using SOI, as we will discuss in Sec. V, can be used to solve the contact problem.

## IV. TRANSPORT MEASUREMENTS

### A. 2D carrier densities vs. gate voltage

Longitudinal ( $R_{xx}$ ) and Hall ( $R_{xy}$ ) resistances were measured at 300 mK using standard low-frequency AC



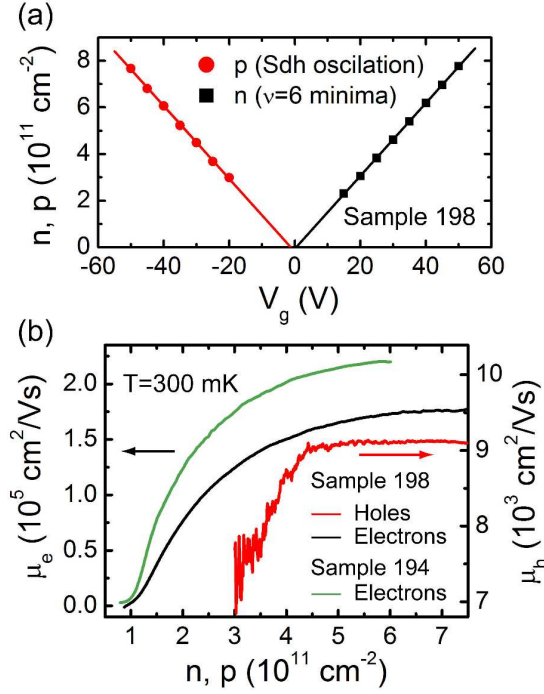


FIG. 10. (a) Electron and hole densities as a function of gate voltage for sample 198. The electron density is determined from the magnetic field of  $R_{xx}$  minima at the filling factor  $\nu = 6$ , and the hole density is calculated from the Shubnikov-de Haas oscillations. (b) 2D carrier mobility of sample 194 and 198 vs. carrier density at 300 mK. For the ambipolar device 198, the ratio between the peak electron and hole mobilities is about 20.

lock-in techniques with an excitation current of 100 nA at 7 Hz. Sheet resistance was determined by standard Van der Pauw method. Magnetotransport measurements were performed at different gate voltages in a perpendicular magnetic field ( $B_{\perp}$ ) up to 12 T. From the SdH oscillations, the 2D hole densities are determined at each gate voltage. The 2D electron densities  $n_{2d}$  are calculated from the magnetic field  $B$  of  $R_{xx}$  minima at the filling factor  $\nu = 6$ :  $n_{2d} = \nu e B / h$ , where  $e$  is the electron charge, and  $h$  is Planck's constant. The 2D densities and their linear fits for sample 198 are shown in Fig. 10(a). For electrons, the slope is  $1.563 \pm 0.004 \times 10^{10} \text{ cm}^{-2}/\text{V}$ , and the threshold voltage is  $V_{e,th} = 0.4 \pm 0.1 \text{ V}$ . For holes, the slope is  $1.566 \pm 0.001 \times 10^{10} \text{ cm}^{-2}/\text{V}$ , and the threshold voltage is  $V_{h,th} = -1.21 \pm 0.03 \text{ V}$ . If a parallel plate capacitor model is used, the equivalent depth of the vacuum cavity is  $355 \pm 1 \text{ nm}$ , which is consistent with the measurement result using a profilometer. The interface trap density in the band gap is determined to be:  $D_{it} \approx (V_{e,th} - V_{h,th} - E_{gap}) \times 1.56 \times 10^{10} \approx 0.8 \times 10^{10} (\text{cm}^{-2})$ , where the band gap  $E_{gap}$  is 1.17 V for silicon at 0 K [48].

## B. 2D carrier mobilities

2D carrier mobilities are calculated from the sheet resistance, and plotted in Fig. 10(b). For sample 194, the peak electron mobility was  $2.2 \times 10^5 \text{ cm}^2/\text{Vs}$  at 300 mK. For sample 198, the peak electron mobility and the peak hole mobility were very different,  $1.76 \times 10^5 \text{ cm}^2/\text{Vs}$  and  $9.1 \times 10^3 \text{ cm}^2/\text{Vs}$  respectively at 300 mK, although the electrons and holes were populated in the same conduction channel. The ratio between the peak electron and hole mobilities is about 20, which cannot be explained by the different effective mass of electrons and holes. In fact, the effective mass is comparable ( $\sim 0.38m_e$  for electrons [3, 49, 50] and  $\sim 0.34m_e$  for holes [51], where  $m_e$  is the electron mass) at the investigated densities. This is quite different from the results of GaAs ambipolar devices, in which the ratio of the peak electron mobility to the peak hole mobility is about 5, consistent with the different effective mass of electrons and holes [22]. The large difference in the electron and hole mobilities is a direct consequence of the very different Coulomb disorder screening strength due to the different valley degeneracies of electrons ( $g_v = 6$ ) and holes ( $g_v = 1$ ) at the Si(111) surface [29].

In addition, the electron mobility increases monotonically with the electron density, and the mobility saturation is not observed up to the highest electron density measured ( $n = 7.8 \times 10^{11} \text{ cm}^{-2}$ ), which is limited by the gate breakdown voltage. From the electron conductivity  $\sigma$  vs. electron density  $n$  data, the fitting exponent  $\alpha$  in the relation of  $\sigma \sim n^{\alpha}$  is about 1.3 at  $n = 7 \times 10^{11} \text{ cm}^{-2}$  in these devices [29], which is consistent with the case ( $\alpha \approx 1.3$ ) where the electron mobility is mainly limited by 3D bulk impurities, while deviating from the case ( $\alpha \approx 1.05$ ) where 2D interface impurities limit the electron mobility [52]. We have developed a rebonding technique, which can revive a sample by taking it apart, cleaning the two pieces and H-passivating the Si(111) piece, then rebonding them together. The piranha cleaning and the diluted HF etching can remove the top few nm of silicon from the Si(111) piece. We tested it on sample 195 with an initial electron mobility of  $5.6 \times 10^4 \text{ cm}^2/\text{Vs}$  at  $n = 6 \times 10^{11} \text{ cm}^{-2}$  and  $T = 300 \text{ mK}$ . After repeated piranha cleaning and diluted HF etching three times, the electron mobility increased to  $7.2 \times 10^4 \text{ cm}^2/\text{Vs}$  ( $n = 6 \times 10^{11} \text{ cm}^{-2}$ ,  $T = 300 \text{ mK}$ ), which is likely due to the removal of the surface layers with higher 3D impurity density from earlier processes. All these suggest that the electron mobility is still mainly limited by 3D bulk impurities for current generation devices.

## C. Magnetotransport measurements

All magnetotransport measurements were carried out in  $B_{\perp}$  in this paper. Figure 11 shows the magnetoresistance for similar electron and hole densities in the same device (sample 198) at  $T = 300 \text{ mK}$ . The frequency of the



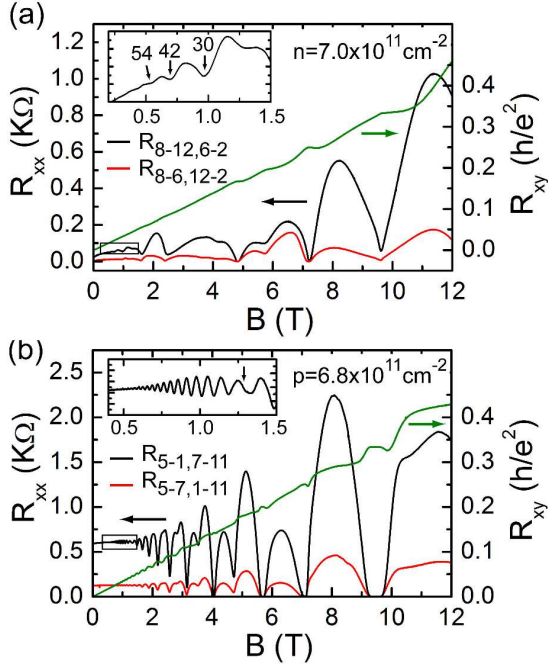


FIG. 11. Magnetoresistance and Hall resistance measured at 300 mK for similar (a) electron and (b) hole densities on sample 198. The frequency of the SdH oscillations is much higher for holes than electrons owing to different valley degeneracy (1:6). The insert in (a) clearly shows the 12-fold periodicity from the sixfold valley degeneracy of the 2DES and the twofold spin degeneracy. The insert in (b) shows a beating pattern with a beating node at the arrow.

SdH oscillations was much higher for holes than electrons at low field, because electrons and holes have different areas of the Fermi surface resulting from the different valley degeneracies. For the 2DHS, the characteristic beating node was observed at  $B = 1.25$  T for  $p_{2d} = 6.8 \times 10^{11} \text{ cm}^{-2}$  [9], and the IQHE was also observed at high field ( $B > 5$  T). For the 2DES, the SdH oscillations began at  $B \approx 0.25$  T, and  $R_{xx}$  minima showed clearly the 12-fold periodicity [the insert of Fig. 11(a)] from the sixfold valley degeneracy and the twofold spin degeneracy. In contrast to previous investigations of Si(111) transport on MOSFETs with peak electron mobility  $\mu \leq 2,500 \text{ cm}^2/\text{Vs}$  which have shown conflicting valley degeneracies of two [50] and six [53], all six current generation H-Si(111) devices with electron mobility of more than  $50,000 \text{ cm}^2/\text{Vs}$  show exclusively the sixfold valley degeneracy at low magnetic field.

#### D. Three magnetoresistance measurements with threefold rotational symmetry

Because electrons have six equivalent valleys on the Si(111) surface, the six  $n^+$  Ohmic contacts are placed along the major axes of the constant energy ellipses, labeled as 2, 4, ..., 12, as shown in Fig. 12 (a)(b). The

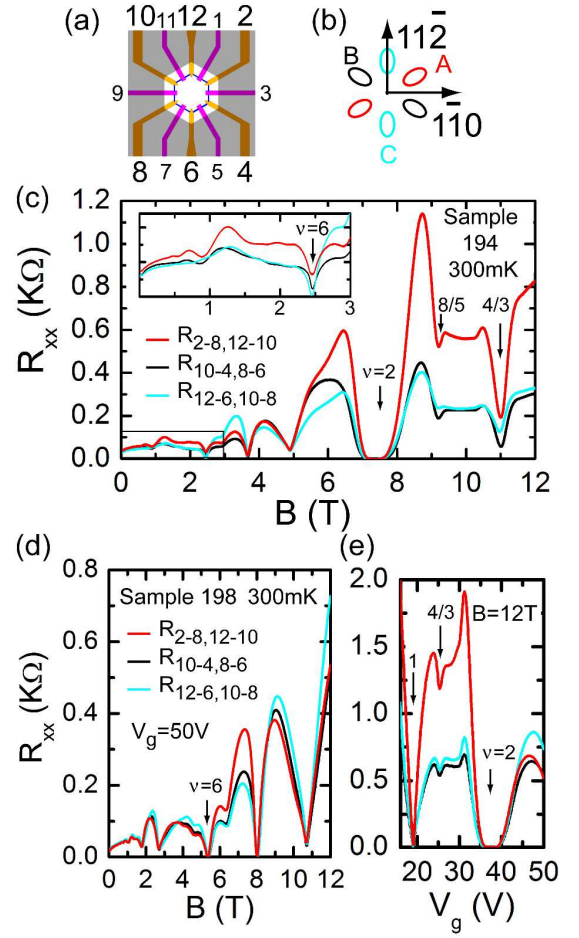


FIG. 12. (a) Top view of a device with six electron contacts and six hole contacts in relation to (b) the 3 pairs of the valleys, labeled as A, B and C. (c) Three magnetoresistance measurements on sample 194 at  $n_{2d} = 3.6 \times 10^{11} \text{ cm}^{-2}$  with the insert showing the low field behavior. (d) (e) Three magnetoresistance measurements on sample 198 at  $n_{2d} = 7.8 \times 10^{11} \text{ cm}^{-2}$ . For both samples 194 and 198, one trace is higher than the other two similar traces at  $1 < \nu < 2$ .

six equivalent valleys form three pairs with opposite momentum, labeled as A, B and C. The degeneracy of valley pairs with  $\pm \vec{k}$  symmetry on the Si(111) surface cannot be broken within the effective mass approximation or by a confinement potential [54, 55]. Similarly, longitudinal magnetoresistance  $R_{xx}$ , measured with current contacts on opposite sides of the hexagonal devices, also has three different directions defined by the direction of current flow. Here four-terminal resistance is defined as  $R_{i-j,l-m} = V_{l-m}/I_{i-j}$  ( $i, j, l, m = 2, 4, \dots, 12$ ), where current  $I_{i-j}$  is injected from contact  $i$  to contact  $j$ , and voltage  $V_{l-m}$  is measured between contacts  $l$  and  $m$ . If the current flows from 2 to 8, it is called trace A ( $R_{2-8,12-10}$ ). If the current flows from 10 to 4, it is called trace B ( $R_{10-4,8-6}$ ), and if the current flows from 12 to 6, it is called trace C ( $R_{12-6,10-8}$ ). These three magnetoresistances  $R_{xx}$  with threefold rotational symmetry

can be used to determine the underlying symmetry of the 2DES, and help identify the valley occupancies of the 2DES. For example, if electrons only occupy valley pair A, trace A will show higher resistance, while trace B and C will show similar lower resistance, due to the different effective mass.

Figure 12(c)-(e) show the three magnetoresistance measurements on sample 194 and 198. Data were taken at 300 mK and a density of  $3.6 \times 10^{11} \text{ cm}^{-2}$  or  $7.8 \times 10^{11} \text{ cm}^{-2}$  for samples 194 and 198 respectively. The two simplest cases are  $B = 0$  and  $B$  at  $\nu = 3/2$  where composite fermions (CFs) experience a zero effective magnetic field. At  $B = 0$ , both devices show more or less isotropic resistances. For sample 194, the three resistances are 37.2  $\Omega$ , 30.4  $\Omega$ , and 30.3  $\Omega$ ; for sample 198, they are 16.0  $\Omega$ , 17.9  $\Omega$ , and 17.9  $\Omega$ , as shown in Fig. 12(c)(d). At  $B_{3/2}$ , the devices are anisotropic. For sample 194, the three magnetoresistances are 558.1  $\Omega$ , 226.3  $\Omega$ , and 232.8  $\Omega$ . For sample 198, they are 1356.9  $\Omega$ , 615.4  $\Omega$ , and 664.7  $\Omega$ . The observed anisotropy can be explained by CFs' occupying valley pair A. Because of the effective mass anisotropy, trace A shows higher resistance, and traces B and C show similar lower resistance. The ratios between the higher and lower resistances are 2.43 and 2.12 for sample 194 and 198 respectively.

In a Drude model with noninteracting electrons, assuming an isotropic scattering time, the resistance ratio is equal to the mass ratio  $m_l/m_t$ , where  $m_l = 0.67m_e$  and  $m_t = 0.19m_e$  [54] are the longitudinal effective mass and the transverse effective mass respectively. For CFs, all physical quantities are determined by the Coulomb interaction [56]. In an isotropic 2DS, the Coulomb interaction is  $\propto 1/\sqrt{x^2 + y^2}$ , where  $x$  and  $y$  are components of the distance between two electrons. According to Ref. 57, in a system with an anisotropic Fermi surface, it can be mapped to a system with an isotropic Fermi surface with an anisotropic Coulomb interaction  $\propto 1/\sqrt{x^2\gamma^2 + y^2/\gamma^2}$ , where  $\gamma = (m_l/m_t)^{1/4}$ ,  $x$  and  $y$  are along the major and minor axes of the constant energy ellipse. If the transport mass of CFs along some direction is determined by the strength of the Coulomb interaction along this direction, the mass-anisotropy ratio of CFs is given by  $\gamma^2 = \sqrt{m_l/m_t}$ . We have calculated two cases using COMSOL assuming the isotropic scattering time: in the first case, the mass-anisotropy ratio of CFs is assumed to be  $m_l/m_t$ ; in the second case, it is assumed to be  $\sqrt{m_l/m_t}$ . Using a hexagonal geometry similar to Fig. 1(c) and assuming the anisotropic resistance solely from the anisotropic effective mass, the calculated ratios between the higher and lower resistances are 3.58 and 2.07 respectively for these two cases. The measured ratios 2.43 and 2.12 fall between these two cases and are closer to the second case. Our results are similar to Ref. 57, but deviate from a theoretical study which predicts almost isotropic CF effective mass [58]. Because the scattering time anisotropy is not well known, the above discussion becomes more complicated. Nevertheless, in a simplest picture, electrons occupy the lowest valley pair at filling

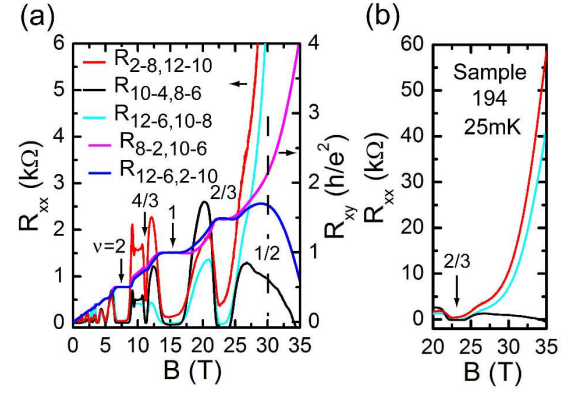


FIG. 13. (a) Three magnetoresistances and Hall resistance measured on sample 194 at 25 mK with the clearly observed  $2/3$  fractional quantum Hall state. (b) The three magnetoresistances are highly anisotropic at  $\nu < 2/3$ , with two similar traces higher than the other one. This may indicate the change of the underlying symmetry.

factor  $1 < \nu < 2$ . Figure 12(c) and (e) show that the corresponding CFs occupy valley pair A, and qualitatively preserve the valley anisotropy, in addition to the twofold valley degeneracy manifested by observed exclusive even numerator fractional quantum Hall (FQH) states ( $8/5$  and  $4/3$ ) [10].

Moreover, at filling factor  $\nu$  between 4 and 6, the devices also show anisotropic magnetoresistances. For sample 194, trace C is highest, while trace A is highest for sample 198. Both cases can be qualitatively explained when the Fermi level is located at valley pair C or valley pair A respectively. For filling factor  $\nu$  between 3 and 4, the three magnetoresistances are similar for both devices, indicating an isotropic distribution of electrons in the three valley pairs. This cannot be explained by a valley occupancy of noninteracting electrons, and may related to the quantum Hall nematic phase [59, 60]. When filling factor  $\nu$  is between 2 and 3, the three magnetoresistances are quite different for sample 194, but similar for sample 198. At lower  $B$  ( $\nu > 6$ ), the three magnetoresistances are similar especially for sample 198, consistent with the approximation that six valleys are equally occupied.

The three magnetoresistance measurements indeed provide a powerful tool to investigate the underlying symmetry of the 2DES on the Si(111) surface. In addition, a tilted magnetic field can re-distribute electrons between the three pairs of valleys through the application of an in-plane magnetic field [54]. If these two techniques are combined, it will further our understanding of this 2DES and the nature of the observed anisotropy.

### E. Magnetotransport measurements up to 35 T

Sample 194 was further investigated at filling factor  $\nu < 1$  in the portable dilution refrigerator (PDF) at NHMFL with a magnetic field up to 35 T. The device was

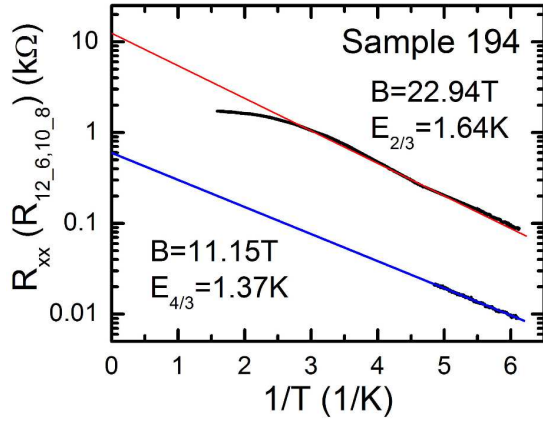


FIG. 14. Arrhenius plots for  $\nu = 2/3, 4/3$  showing activated behavior on sample 194.

measured at  $T = 25$  mK and density of  $3.6 \times 10^{11} \text{ cm}^{-2}$ . As shown in Fig. 13(a), the  $2/3$  FQH state is clearly observed with a well developed hall plateau. Moreover, Fig. 13(b) shows that the three magnetoresistances are highly anisotropic at  $\nu < 2/3$ . It is less than  $1 \text{ k}\Omega$  along trace B, and about  $50 \text{ k}\Omega$  along traces A and C. This 50:1 anisotropy cannot arise solely from the different effective mass. The three magnetoresistances also change from one higher resistance trace with two similar lower resistance traces at  $\nu > 2/3$ , to two similar higher resistance traces with one lower resistance trace at  $\nu < 2/3$ . This may indicate the change of the underlying symmetry of the 2DES.

At filling factor  $\nu$  between 1 and 2, only even numerator FQH states ( $8/5$  and  $4/3$ ) are observed with no  $5/3$  FQH state, consistent with twofold valley-degenerate CFs [10]. It is quite interesting to find out the underlying symmetry of the  $2/3$  FQH state, i.e. whether it also has the twofold valley degeneracy. Because valley degenerate  $2/3$  FQH state may be related to non-Abelian states which are being intensively studied for possible applications in intrinsically fault tolerant quantum computation [61–64], the question becomes more important. We have determined the activation energies at  $\nu = 2/3$  and  $4/3$  from the temperature dependence of magnetoresistance  $R_{xx}$  (Fig. 14). The activation energies are comparable,  $1.64 \text{ K}$  for  $\nu = 2/3$  and  $1.34 \text{ K}$  for  $\nu = 4/3$ . In a twofold valley-degenerate system,  $4/3 (= 2 - 2/3)$  state can be related to  $2/3$  state by using particle-hole symmetry [10, 56, 65, 66]; their activation energies are proportional to  $\sqrt{B}$ , and  $E_{2/3}/E_{4/3} = \sqrt{22.94/11.15} = 1.4$ . The measured ratio is about 1.2, which may imply that the  $2/3$  FQH state also has the twofold valley degeneracy.

## V. DEVICE DEGRADATION

The H-Si(111) surface is encapsulated in a vacuum cavity in the H-Si(111) vacuum FET [Fig. 1(a)], but the

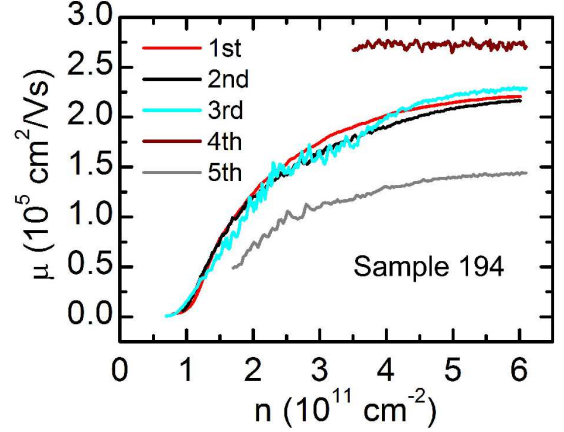


FIG. 15. Electron mobility of sample 194 vs. electron density during five cooldowns, measured at 300 mK except the 4th cooldown (at 25 mK). There was one week of air exposure between the 4th and 5th cooldowns.

seal is not perfectly hermetic. Consequently H-Si(111) vacuum FETs still suffer from device degradation in air owing to degradation of H-terminated surfaces [67–69], which may limit their applications. However, if care is taken to limit the time of the device spent in air, while keeping it mostly in vacuum or a nitrogen gas environment, the device degradation is manageable.

The degradation of the two devices has been recorded. Sample 194 was cooled down five times in a period of 246 days, as shown in Fig. 15. The mobility was mostly measured at 300 mK, except the fourth cooldown (at 25 mK). As described in Sec. II, after the device was bonded and wired in the nitrogen glove box, it was rapidly loaded into the cryostat at the first cooldown. There was about one hour exposure in air before pumping down the cryostat at each cooldown. After the device was measured for about two weeks, it was warmed up, put into a nitrogen gas filled barrier foil ziplock storage bag with oxygen absorbers, and then the bag was heat sealed. After one week, it was cooled down and measured a second time at day 26. Figure 15 shows that the change of the peak electron mobility was about 2%. The device was then warmed up and stored in a nitrogen glove box ( $\text{O}_2 < 10 \text{ ppm}$ ) for about 6 months. Right before transferring the device to the NHMFL, the device was measured a third time. The peak electron mobility increased by about 3%, which may be due to the different temperatures or the different contact resistances. So within 211 days, the device mobility did not change much when keeping it mostly in a nitrogen gas environment. However, the mobility fluctuations were pronounced at lower electron densities at the third cooldown, which was caused by the degradation of the contacts. For transport to NHFML, the device was again placed in a nitrogen gas filled storage bag, as described above. After the NHMFL experiment, the device was exposed in air for about one week, and the peak electron mobility decreased by 35% at the fifth cooldown.



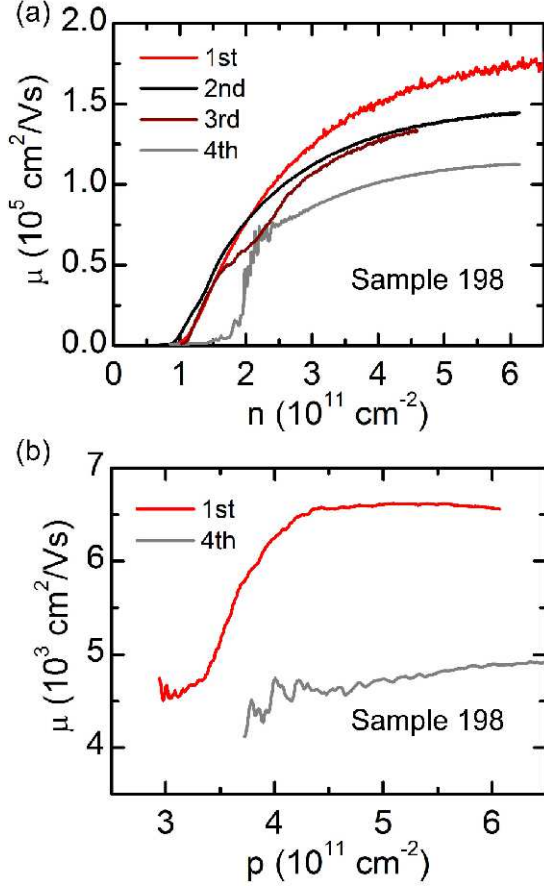


FIG. 16. (a) Electron mobility of sample 198 as a function of electron density during four cooldowns, measured at 300 mK except the 3rd cooldown (at 25 mK). One week air exposure happened between the 3rd and 4th cooldowns. (b) Hole mobility of sample 198 vs. hole density at 1st and 4th cooldowns, measured at 4.2 K.

Similarly, sample 198 was cooled down four times in 193 days, as shown in Fig. 16. After the first measurement, the device was stored in the nitrogen glove box for about 3 months. The peak electron mobility decreased by about 17% at the second cooldown, which degraded faster than that of sample 194. After the same NHMFL experiment, the device was in air for about one week, and the peak electron mobility decreased by another 18% at the fourth cooldown. The hole mobility was decreased by about 26% between the first and fourth cooldown, measured at 4.2 K [Fig. 16(b)].

After  $\sim 200$  days, the peak electron mobility decreased by about 35% for both devices. After one week exposure in air, the peak electron mobility decreased by about 35% and 18% for sample 194 and 198 respectively. Roughly it can be estimated that the peak electron mobility decreased by  $\sim 0.2\%$ /day in vacuum or a nitrogen gas environment, and by  $\sim 5\%$ /day in air.

In addition to the mobility degradation, the contacts also degrade with time. The contact degradation makes accurate resistance measurements difficult, and shows up

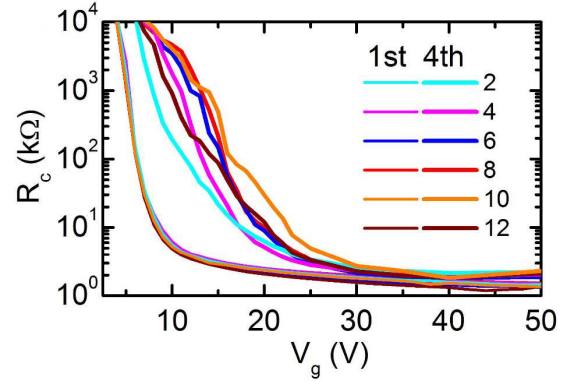


FIG. 17.  $N^+$  contact resistance  $R_c$  as a function of gate voltage  $V_g$  on sample 198 at 300 mK. For 4th cooldown, at  $V_g < 15$  V,  $R_c$  is calculated when  $|I_{ds}| \leq 4$  nA; otherwise,  $R_c$  is determined at  $|I_{ds}| \leq 100$  nA. Compared to 1st cooldown, the contact resistance increased dramatically at low electron density ( $5 < V_g < 25$  V).

as the conductance (mobility) fluctuations both for electrons and holes at lower densities [9, 38]. In sample 198 (without STI), the contact problem had been mitigated, but it resurfaced at the 4th cooldown. The contacts were linear only at above  $V_g = 16$  V ( $n_{2d} = 2.5 \times 10^{11} \text{ cm}^{-2}$ ) rather than  $V_g = 6$  V ( $n_{2d} = 1.02 \times 10^{11} \text{ cm}^{-2}$ ) at the first cooldown, and the contact resistances were also much worse than those at the 1st cooldown (Fig. 17). Correspondingly, the mobility fluctuated at  $n_{2d} < 2.5 \times 10^{11} \text{ cm}^{-2}$  for the 4th cooldown in Fig. 16(a).

Although resistance measurements are possible with pure large contact resistances ( $\sim 10 \text{ M}\Omega$ ) using 4-terminal DC method, there probably exist charge trapping and emission processes in these devices like single electron transistors [38]. The 4-terminal DC method is not effective in this case. In order to solve the contact problem, the bi-layer gate structure using SOI, as shown in Fig. 18 can be adopted. Similar to a split-gate geometry, the bi-layer gate structure which permits high densities around the contacts while allowing independent control of the density of the 2DSs under investigation [70], is quite important going forward.

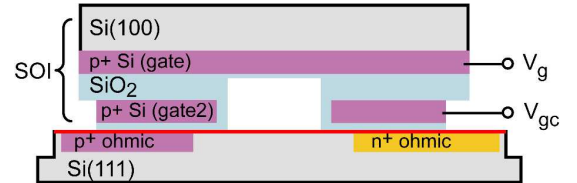


FIG. 18. A vacuum FET with a bi-layer gate structure using SOI. The 2D carrier densities around the contacts and at the investigated area can be independently controlled. The gate is also fully covered by a SiO<sub>2</sub> layer.



## VI. PROSPECTS AND CONCLUSIONS

We have investigated a process to fabricate high mobility ambipolar H-Si(111) vacuum FETs with electron mobility of  $\sim 200,000 \text{ cm}^2/\text{Vs}$  and hole mobility of  $\sim 10,000 \text{ cm}^2/\text{Vs}$ . From the electron conductivity vs. electron density analysis, the electron mobility is still mainly limited by 3D bulk impurities, which implies that the mobility can be further improved with attention to high temperature steps. At a minimum, electron mobility of  $\sim 300,000 \text{ cm}^2/\text{Vs}$  should be able to realize in the near future, since we have already fabricated a device with this mobility using previous sample fabrication techniques [10]. Combined with a bi-layer gate structure to solve the contact issue, the device quality should be comparable to the best SiGe quantum well devices. In addition, the 2DES has a sixfold valley degeneracy, which will open up many opportunities for fundamental research and practical applications.

Three magnetoresistance measurements are a very useful tool to determine the underlying symmetry of the 2DES. They can be used to detect possible phase transition when the associate symmetry changes [59, 60]. Further experiments with a tilted magnetic field to re-distribute electrons between valleys can dynamically change the underlying symmetry. It will surely improve our understanding of this 2DES and the nature of the observed anisotropy.

The devices were also investigated at filling factor  $\nu < 1$  in a magnetic field up to 35 T. We clearly observed the  $2/3$  FQH state with a well developed hall plateau, and a high magnetoresistance anisotropy at  $\nu < 2/3$  on both sample 194 and 198. On sample 194, there were some hints of possible  $3/5$ ,  $4/7$ ,  $5/9$  and  $6/11$  FQH states (data not shown). With better devices, we should be able to verify these additional states. It is quite possible to observe new phases in this unique sixfold valley-degenerate system.

Because of the distinct device structure, the 2D systems are resident at the surface in the vacuum cavity. Atoms, molecules, superconductors and other systems can easily couple to the 2DSs and form hybrid systems [6], and novel functional devices can be implemented in the future.

## ACKNOWLEDGMENTS

This work was funded by the Laboratory for Physical Sciences. Research was performed in part at the NIST Center for Nanoscale Science and Technology, and the National High Magnetic Field Laboratory, which is supported by National Science Foundation Cooperative Agreement No. DMR-1157490 and the State of Florida. We also acknowledge the support of the Maryland NanoCenter and its FabLab. The authors are grateful to Dr. Neil Zimmerman and Dr. Michael Stewart for their help on the RTA process.

- 
- [1] T. Ando, A. B. Fowler, and F. Stern, *Rev. Mod. Phys.* **54**, 437 (1982), and references therein.
  - [2] A. Lakhani and P. Stiles, *Phys. Lett. A* **51**, 117 (1975).
  - [3] T. Neugebauer, K. von Klitzing, G. Landwehr, and G. Dorda, *Solid State Commun.* **17**, 295 (1975).
  - [4] K. von Klitzing, G. Landwehr, and G. Dorda, *Solid State Commun.* **14**, 387 (1974).
  - [5] K. von Klitzing, G. Landwehr, and G. Dorda, *Solid State Commun.* **15**, 489 (1974).
  - [6] K. Eng, R. N. McFarland, and B. E. Kane, *Appl. Phys. Lett.* **87**, 052106 (2005).
  - [7] K. Eng, R. N. McFarland, and B. E. Kane, *Phys. Rev. Lett.* **99**, 016801 (2007).
  - [8] R. N. McFarland, T. M. Kott, L. Sun, K. Eng, and B. E. Kane, *Phys. Rev. B* **80**, 161310 (2009).
  - [9] B. Hu, T. M. Kott, R. N. McFarland, and B. E. Kane, *Appl. Phys. Lett.* **100**, 252107 (2012).
  - [10] T. M. Kott, B. Hu, S. H. Brown, and B. E. Kane, *Phys. Rev. B* **89**, 041107 (2014).
  - [11] G. S. Higashi, Y. J. Chabal, G. W. Trucks, and K. Raghavachari, *Appl. Phys. Lett.* **56** (1990).
  - [12] P. Jakob and Y. J. Chabal, *J. Chem. Phys.* **95** (1991).
  - [13] B. R. Weinberger, H. W. Deckman, E. Yablonovitch, T. Gmitter, W. Kobasz, and S. Garoff, *J. Vac. Sci. Technol. A* **3** (1985).
  - [14] E. Yablonovitch, D. L. Allara, C. C. Chang, T. Gmitter, and T. B. Bright, *Phys. Rev. Lett.* **57**, 249 (1986).
  - [15] F. Schäffler, *Semicond. Sci. Technol.* **12**, 1515 (1997).
  - [16] K. Lai, W. Pan, D. C. Tsui, S. Lyon, M. Mühlberger, and F. Schäffler, *Phys. Rev. Lett.* **93**, 156805 (2004).
  - [17] T. M. Lu, W. Pan, D. C. Tsui, C.-H. Lee, and C. W. Liu, *Phys. Rev. B* **85**, 121307 (2012).
  - [18] T. E. Whall, A. D. Plews, N. L. Matthey, and E. H. C. Parker, *Appl. Phys. Lett.* **65**, 3362 (1994).
  - [19] E. Basaran, R. A. Kubiak, T. E. Whall, and E. H. C. Parker, *Appl. Phys. Lett.* **64**, 3470 (1994).
  - [20] M. L. Lee, D. A. Antoniadis, and E. A. Fitzgerald, *Thin Solid Films* **508**, 136 (2006).
  - [21] E. Gatti, F. Isa, D. Chrastina, E. Müller Gubler, F. Pezzoli, E. Grilli, and G. Isella, *J. Appl. Phys.* **116**, 043518 (2014).
  - [22] J. C. H. Chen, D. Q. Wang, O. Klochan, A. P. Micolich, K. Das Gupta, F. Sfigakis, D. A. Ritchie, D. Reuter, A. D. Wieck, and A. R. Hamilton, *Appl. Phys. Lett.* **100**, 052101 (2012).
  - [23] A. F. Croxall, B. Zheng, F. Sfigakis, K. Das Gupta, I. Farrer, C. A. Nicoll, H. E. Beere, and D. A. Ritchie, *Appl. Phys. Lett.* **102**, 082105 (2013).
  - [24] K. Novoselov, A. K. Geim, S. Morozov, D. Jiang, M. Katsnelson, I. Grigorieva, S. Dubonos, and A. Firsov, *nature* **438**, 197 (2005).
  - [25] J. F. Tian, L. A. Jauregui, G. Lopez, H. Cao, and Y. P. Chen, *Appl. Phys. Lett.* **96**, 263110 (2010).
  - [26] S. Das, M. Demarteau, and A. Roelofs, *ACS Nano* **8**,

- 11730 (2014).
- [27] A. C. Betz, M. F. Gonzalez-Zalba, G. Podd, and A. J. Ferguson, *Appl. Phys. Lett.* **105**, 153113 (2014).
  - [28] F. Mueller, G. Konstantaras, W. G. van der Wiel, and F. A. Zwanenburg, *Appl. Phys. Lett.* **106**, 172101 (2015).
  - [29] B. Hu, M. M. Yazdanpanah, B. E. Kane, E. H. Hwang, and S. Das Sarma, *Phys. Rev. Lett.* **115**, 036801 (2015).
  - [30] H. Zeng, J. Dai, W. Yao, D. Xiao, and X. Cui, *Nat. Nanotechnol.* **7**, 490 (2012).
  - [31] J. Isberg, M. Gabrysch, J. Hammersberg, S. Majdi, K. K. Kovi, and D. J. Twitchen, *Nat. Mater.* **12**, 760 (2013).
  - [32] V. Renard, B. Piot, X. Waintal, G. Fleury, D. Cooper, Y. Niida, D. Tregurtha, A. Fujiwara, Y. Hirayama, and K. Takashina, *Nat. Commun.* **6** (2015).
  - [33] SEMI International standards, SEMI M1-0298.
  - [34] SUPREM-IV computer code was developed by R. W. Dutton and J. D. Plummer at the Integrated Circuits Laboratory, Stanford University.
  - [35] T. F. Rosenbaum, K. Andres, G. A. Thomas, and R. N. Bhatt, *Phys. Rev. Lett.* **45**, 1723 (1980).
  - [36] P. Dai, Y. Zhang, and M. P. Sarachik, *Phys. Rev. Lett.* **66**, 1914 (1991).
  - [37] C. P. Wade and C. E. D. Chidsey, *Appl. Phys. Lett.* **71** (1997).
  - [38] T. M. Kott, *Measurements of Correlated 2D Electrons in the Lowest Landau Level on Silicon-(111)*, Ph.D. thesis, University of Maryland, College Park (2012).
  - [39] R. N. McFarland, *Multi-Valley Physics of Two-Dimensional Electron Systemson Hydrogen-Terminated Silicon (111) Surfaces*, Ph.D. thesis, University of Maryland, College Park (2010).
  - [40] E. H. Hwang and S. Das Sarma, *Phys. Rev. B* **75**, 073301 (2007).
  - [41] E. H. Hwang and S. Das Sarma, *Phys. Rev. B* **87**, 075306 (2013).
  - [42] <http://www.comsol.com/>.
  - [43] S. V. Kravchenko and M. P. Sarachik, *Rep. Prog. Phys.* **67**, 1 (2004), and references therein.
  - [44] J. D. Plummer, M. Deal, and P. D. Griffin, *Silicon VLSI technology: fundamentals, practice, and modeling* (Pearson Education, 2000).
  - [45] F. Morehead Jr and B. Crowder, *Radiat. Eff.* **6**, 27 (1970).
  - [46] S. Furukawa, H. Matsumura, and H. Ishiware, *Jpn. J. Appl. Phys.* **11**, 134 (1972).
  - [47] V. Privitera, V. Raineri, M. Saggio, F. Priolo, and E. Rimini, *Nucl. Instrum. Methods Phys. Res., Sect. B* **96**, 144 (1995).
  - [48] S. M. Sze, *Physics of semiconductor devices* (John Wiley & Sons, 1981).
  - [49] G. Abstreiter, J. P. Kotthaus, J. F. Koch, and G. Dorda, *Phys. Rev. B* **14**, 2480 (1976).
  - [50] A. A. Shashkin, A. A. Kapustin, E. V. Deviatov, V. T. Dolgoplov, and Z. D. Kvon, *Phys. Rev. B* **76**, 241302 (2007).
  - [51] J. P. Kotthaus and R. Ranvaud, *Phys. Rev. B* **15**, 5758 (1977).
  - [52] Internal communication with E. H. Hwang and S. Das Sarma; see also S. Das Sarma and E. H. Hwang, *Phys. Rev. B* **88**, 035439 (2013).
  - [53] D. C. Tsui and G. Kaminsky, *Phys. Rev. Lett.* **42**, 595 (1979).
  - [54] F. Stern and W. E. Howard, *Phys. Rev.* **163**, 816 (1967).
  - [55] M. Rasolt, B. I. Halperin, and D. Vanderbilt, *Phys. Rev. Lett.* **57**, 126 (1986).
  - [56] J. K. Jain, *Composite Fermions* (Cambridge University Press, 2007).
  - [57] T. Gokmen, M. Padmanabhan, and M. Shayegan, *Nat. Phys.* **6**, 621 (2010).
  - [58] D. B. Balagurov and Y. E. Lozovik, *Phys. Rev. B* **62**, 1481 (2000).
  - [59] D. A. Abanin, S. A. Parameswaran, S. A. Kivelson, and S. L. Sondhi, *Phys. Rev. B* **82**, 035428 (2010).
  - [60] A. Kumar, S. Parameswaran, and S. Sondhi, *arXiv:1411.3354* (2014).
  - [61] S. Geraedts, M. P. Zaletel, Z. Papić, and R. S. K. Mong, *Phys. Rev. B* **91**, 205139 (2015).
  - [62] M. R. Peterson, Y.-L. Wu, M. Cheng, M. Barkeshli, Z. Wang, and S. Das Sarma, *Phys. Rev. B* **92**, 035103 (2015).
  - [63] W. Zhu, S. S. Gong, D. N. Sheng, and L. Sheng, *Phys. Rev. B* **91**, 245126 (2015).
  - [64] Z. Liu, A. Vaezi, K. Lee, and E.-A. Kim, *arXiv preprint arXiv:1502.05391* (2015).
  - [65] G. S. Boebinger, A. M. Chang, H. L. Stormer, and D. C. Tsui, *Phys. Rev. Lett.* **55**, 1606 (1985).
  - [66] K. Park and J. Jain, *Solid State Commun.* **119**, 291 (2001).
  - [67] F. Grey and K. Hermansson, *Appl. Phys. Lett.* **71** (1997).
  - [68] W. J. Royea, A. Juang, and N. S. Lewis, *Appl. Phys. Lett.* **77** (2000).
  - [69] L. J. Webb, , and N. S. Lewis, *J. Phys. Chem. B* **107**, 5404 (2003).
  - [70] S. A. Vitkalov, H. Zheng, K. M. Mertes, M. P. Sarachik, and T. M. Klapwijk, *Phys. Rev. Lett.* **85**, 2164 (2000). The idea of bi-layer gate structure using SOI is from the discussion with Alex R. Hamilton of University of New South Wales, Australia.